Volume 143 | Number 12 | 21 June 2018 | Pages 2707–2924

Analyst

rsc.li/analyst

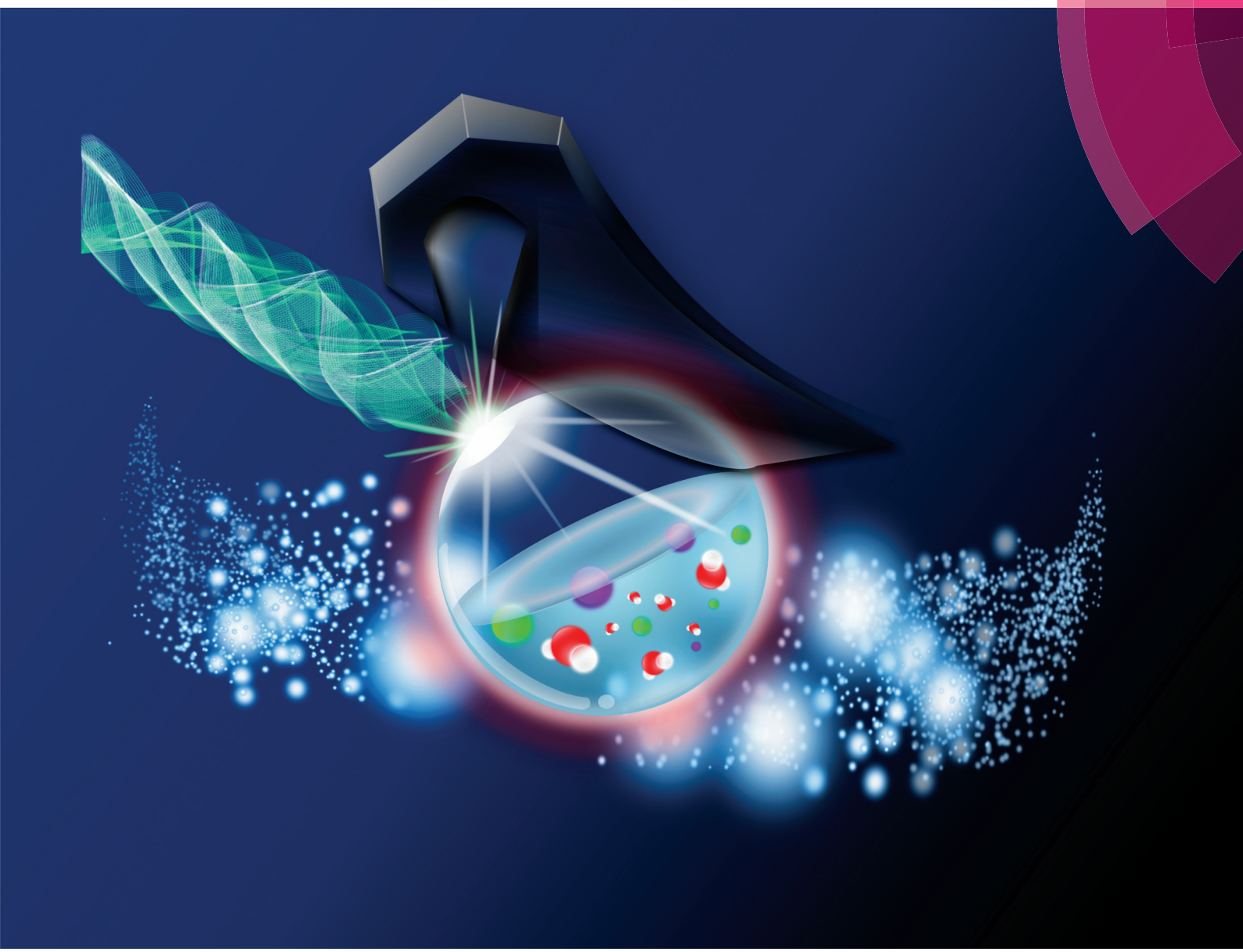

ISSN 0003-2654

ROYAL SOCIETY OF CHEMISTRY

PAPER

Vicki H. Grassian, Alexei V. Tivanski *et al.*

Lab on a tip: atomic force microscopy – photothermal infrared spectroscopy of atmospherically relevant organic/inorganic aerosol particles in the nanometer to micrometer size range

Analyst

PAPER

View Article Online
View Journal | View Issue

Check for updates

Cite this: *Analyst*, 2018, **143**, 2765

Lab on a tip: atomic force microscopy – photothermal infrared spectroscopy of atmospherically relevant organic/inorganic aerosol particles in the nanometer to micrometer size range†

Victor W. Or, [a] Armando D. Estillore, [a] Alexei V. Tivanski*[b] and Vicki H. Grassian *[a,c]

New developments in nanoscale analytical techniques have paved the way for detailed spectroscopic and microscopic measurements of substrate-deposited aerosol particles on a single particle basis. Atomic force microscopy based photothermal infrared (AFM-PTIR) spectroscopy is a technique that combines the nanometer spatial resolution of AFM with the chemical analysis capabilities of vibrational IR spectroscopy. Herein we demonstrate the capability of AFM-PTIR to investigate single and multi-component systems comprised of inorganic salts and organic compounds relevant to the atmosphere. Chemical and microscopic characterization of individual particles as small as 50 nm in diameter is shown. Moreover, single particle spectro-microscopic characterization as a function of relative humidity using this technique is shown for the first time. These new measurements as a function of relative humidity allow for the simultaneous and independent acquisition of photothermal IR spectra, contact resonance frequency shifts, and water uptake growth factors, providing insight on changes in the composition, stiffness, and size of the particles, respectively. These results lay the foundation for more detailed AFM-PTIR studies of multi-component aerosol particles under a range of environmental conditions.

Received 28th January 2018,
Accepted 23rd March 2018

DOI: 10.1039/c8an00171e

rsc.li/analyst

Published on 28 March 2018. Downloaded on 5/5/2026 1:00:26 AM.

1. Introduction

Earth's atmosphere contains suspended liquid and solid particles called aerosols, which are directly emitted from a variety of sources (primary aerosols) or formed in the atmosphere through gas-to-particle conversion processes (secondary aerosols).[1–3] The interaction of atmospheric aerosols with solar radiation is complex, and the quantitative impacts of aerosols on climate and environment have many uncertainties due to different physicochemical properties such as their size, reactivity, and affinity to interact with water vapor to form clouds.[4–7] In addition, human exposure to aerosol particles have been linked to a variety of health effects.[8–12]

Several recent field campaigns report variation in the chemical composition and morphology of individual particles, which reflects diversity in particle emission sources.[13–17] A single aerosol particle typically consists of a mixture of components; with many aerosols containing both organic compounds and inorganic salts. The presence of organic compounds within inorganic salt aerosols in a mixed state can strongly alter the chemical reactivity and physical properties of the aerosol.[18] Thus, increasing interest has been placed on studying the composition, morphology, and phase state of aerosol particles comprised of both organic compounds and inorganic salts. Adding to this complexity, the components within the particle can vary in mixing states, resulting in different internal and external morphologies and corresponding phase states.[19–21] Morphology, phase, and chemical composition are the vital links to understanding the impacts of aerosol particles in the atmosphere, and there is a need for detailed studies of individual particles under realistic atmospheric conditions.

Atomic force microscopy (AFM) is an attractive and non-destructive method that permits visualization of the microscopic details of a particle with nanoscale spatial resolution at ambient conditions.[22,23] Table 1 summarizes some of the important recent advances by Tivanski, Grassian and co-

[a]*Department of Chemistry and Biochemistry, University of California San Diego, La Jolla, CA 92093, USA. E-mail: vhgrassian@ucsd.edu; Tel: +(858)-534-2499*
[b]*Department of Chemistry, University of Iowa, Iowa City, Iowa 52242, USA. E-mail: alexei-tivanski@uiowa.edu; Tel: +(319)-384-1865*
[c]*Scripps Institution of Oceanography and Department of Nanoengineering, University of California, San Diego, La Jolla, CA 92093, USA*

†Electronic supplementary information (ESI) available. See DOI: 10.1039/C8AN00171E. The data used to generate the figures and conclusions in this paper are included in a dataset hosted by the UCSD Library Digital Collections DOI: 10.6075/J0F47MBF

Published on 28 March 2018. Downloaded on 5/5/2026 1:00:26 AM.

Table 1 Aerosol particle properties that can be measured using AFM compared to AFM-PTIR spectroscopy

Property	Parameter	AFM	AFM-PTIR
Morphology 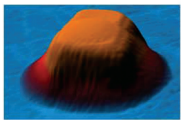	*Particle size*: High resolution of a single particle's height, deposited diameter, and volume equivalent diameter.	✓	✓
	Particle shape: Measure the relative geometric shape of the deposited particles (asphericity, aggregates, *etc.*)	✓	✓
	Mixing state: Examines phase separations within particles (core–shell, partially engulfed, *etc.*) and the relative organic coating (organic volume fraction)	✓	✓
	Aspect ratio: Measures the relative degree of particle deformation after being impacted on the substrate by taking the ratio of the deposited height *vs.* diameter.	✓	✓
	Reaction rates: Measure time dependent morphological and physical changes of particles exposed to reactive gases	✓	✓
Mechanical Properties 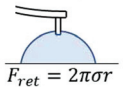	*Adhesion interactions*: Interaction forces between a functionalized cantilever and a surface of interest as a function of sample–tip separation	✓	✓
	Dissolution: Imaging of aerosol particles in various solvents as a function of time	✓	✓
	Surface tension: Measures the retention force between a constant diameter nanoneedle and a liquid particle	✓	✓
	Frequency mapping: Spatial distribution of the contact resonance frequencies between the tip and sample, which shift as a function of sample stiffness	✓	✓
Chemical Characterization 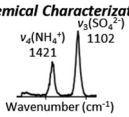	*Reaction rates*: Measure time dependent spectral changes in particles exposed to reactive gases	✗	✓
	Chemical mapping: Spatial distribution of the photothermal induced resonance between the tip and sample	✗	✓
	PTIR spectroscopy: Cantilever localized detection of particle absorption of infrared radiation, *via* temperature increase and subsequent expansion	✗	✓
Hygroscopicity 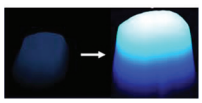	*Hygroscopic growth factor*: Compares volume equivalent diameters for substrate deposited particles as a function of relative humidity.	✓	✓
	Phase state: Examines viscoelastic response distance and relative indentation depth of the nanoneedle with the particle to determine phase state and transitions.	✓	✓
	Resonance frequency shifts: Measures shifts in the contact resonance frequency as the particle softens or hardens due to water intake or release.	✓	✓
	Spectroscopic changes: Localized PTIR spectroscopy observes the chemical signature changes within the particle due to water uptake or loss.	✓	✓

workers in using AFM to investigate atmospherically relevant particles including accurate measurements of particle size, three-dimensional (3D) structure, morphology, phase, 3D growth factors, organic to salt volume fraction ratio for mixed particles, and surface tension force measurements as a function of relative humidity.[24–27] While AFM can probe the structural detail and physicochemical properties of individual atmospheric particles, it cannot directly provide chemical information about the particle. What remains a grand challenge in aerosol research is the simultaneous measurements of the chemical composition, morphology, and properties of individual aerosol particle especially in the nanometer size range, a size regime important for atmospheric chemistry,[28] health and climate.[29,30]

Atomic force microscopy based photothermal infrared (AFM-PTIR) spectroscopy is a photothermal induced resonance (PTIR) technique that combines the high spatial resolution of AFM with the chemical analysis capabilities of vibrational spectroscopy.[31–33] Briefly, the technique converts thermal expansion which originates from the absorption of infrared radiation, into cantilever displacement, generating a signal proportional to the amount of IR light absorbed. Because the displacement measured is localized to the cantilever tip, AFM-PTIR allows chemical analysis with spatial resolution well below the diffraction limit. AFM-PTIR has been successfully employed in various fields, including polymers, life, medical, and material sciences.[31] More recently, Bondy *et al.* have demonstrated AFM-PTIR spectroscopy to investigate atmospherically relevant aerosol particles, but noted issues such as low deflection signal from photothermal particle expansion, especially for small particles below 200 nm, and differing peak-to-peak ratios compared to Fourier Transform Infrared (FTIR) spectroscopy.[34]

Thus, there remains a need to further develop AFM-PTIR spectroscopy as a quantitative tool for analysing substrate-deposited aerosol particles. Herein, we use AFM-PTIR to measure the particle morphology and the associated chemical information of several model aerosol particles on a single particle basis. We present results for the infrared spectroscopic characterization of single component aerosol particles, including ammonium sulfate (AS) particles as small as 50 nm in diameter. Such small size range is important due to relatively high abundance of particles below 100 nm in the troposphere and their importance as cloud condensation nuclei and ice nucleators.[29,35,36] In addition, we provide similar characterization of particles as large as 2.6 microns in diameter. Previous studies have shown supermicron sized particles contribute to a significant fraction of total ice nucleators (IN).[35] To further demonstrate AFM-PTIR as a technique for studying particles comprised of components that vary in both chemical and physical properties, we present results for two component model aerosols comprised of an organic compound, (pimelic acid (PA) and glucose) and an inorganic salt, (sodium chloride and ammonium sulfate). These were selected as important

 This journal is © The Royal Society of Chemistry 2018

Published on 28 March 2018. Downloaded on 5/5/2026 1:00:26 AM.

model systems of tropospheric aerosol particles which are comprised of sea salt, inorganic sulfates, dicarboxylic acids, and saccharides. We also show results for collecting AFM-PTIR images and spectra of a single particle as a function of relative humidity for the first time. A summary table of the advancement in capabilities for aerosol studies using the AFM-PTIR method is provided in Table 1. When compared to a standalone AFM, AFM-PTIR spectroscopy gives information on the samples mechanical and spectroscopic changes that can be coupled with the imaging and tip-probe measurements from AFM to give a more complete picture of the behaviour of aerosol particles in the submicron size regime.

2. Experimental Methods

2.1. Materials

All chemicals used were purchased directly from the manufacturers, utilized without further purification, and included ammonium sulfate ($(NH_4)_2SO_4$, >99%, Fischer Scientific), sodium chloride (NaCl, ≥99%, Fischer Scientific), glucose ($C_6H_{12}O_6$, ≥99.0%, Sigma-Aldrich), sodium nitrate ($NaNO_3$, ≥99%, Sigma-Aldrich), pimelic acid ($C_7H_{12}O_4$, ≥99.0%, Sigma-Aldrich). Single component aerosol particles were generated from a 0.5 or 1% wt/v aqueous solution using ultrapure water prepared on site (Thermo, Barnsted EasyPure-II; ≥18.2 MΩ cm resistivity). Aqueous solutions of compounds (and 1 : 1 wt% mixtures) listed above were atomized (TSI Inc., model 3076) to generate the aerosol particles. The aerosol particles were then sent through two diffusion dryers (TSI Inc., model 3062) at a flow rate of 1.5 lpm to reduce the RH to *ca.* 5% RH. Zinc sulfide (ZnS) and Si wafer sampling substrates (Ted Pella) were used to collect the aerosol particles by mounting the substrate in front of an electrostatic classifier (TSI Inc., model 3080) for 1–10 min. Due to the thickness of the ZnS substrate, samples could not fit in a MOUDI or CASCADE size selector. For relative humidity studies, hydrophobic substrates were prepared by cleaning Si wafer sampling substrates with isopropanol and coating in commercially available Rain-X.[37,38]

2.2. Atomic force microscopy – photothermal infrared spectroscopy

Samples were analyzed using a commercial nanoIR2 microscopy system (Anasys Instruments, Santa Barbara, CA, USA). The instrument consists of an atomic force microscope integrated with a pulsed, tunable infrared optical parametric oscillator (OPO) laser source with repetition rate of 1 kHz, tuning range of 850 to 2000 cm^{-1} and 2235 to 3600 cm^{-1}, and an average spectral resolution of 4 cm^{-1}. The sample is irradiated with a pulsed IR laser radiation in a top-down fashion, as shown in Fig. 1a, with a spot size of ~30 μm. The pulsed radiation is selectively absorbed by the sample, causing rapid and transient thermal expansion, which is locally detected by the resulting mechanical deflection change of the AFM probe. The deflection signal is divided by the background level of the IR source at each wavenumber to remove effects of power

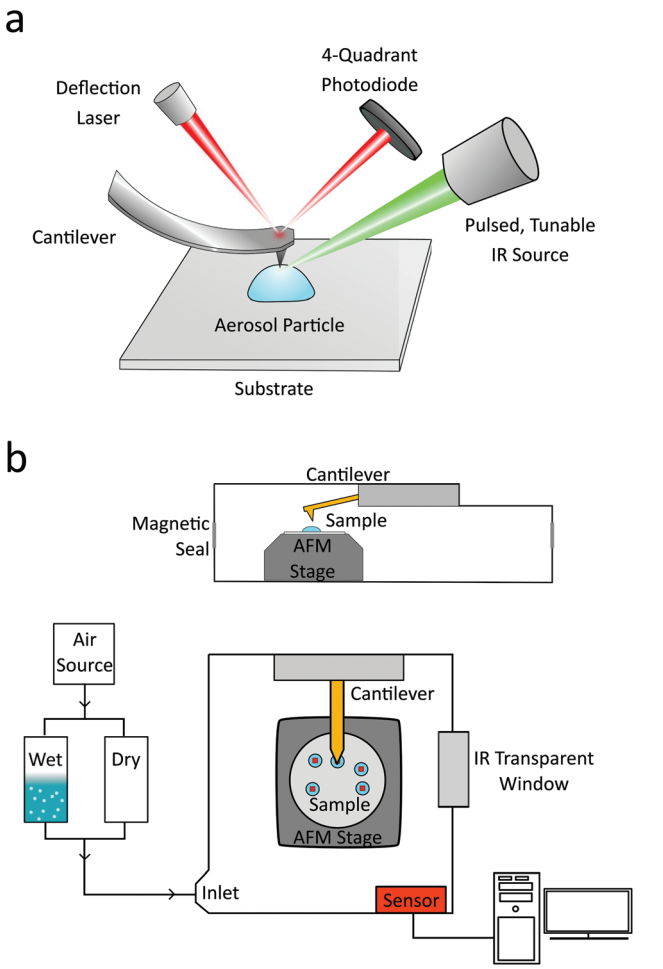

Fig. 1 (a) An illustrative representation of the main AFM-PTIR components is shown in the overhead configuration. (b) Schematic of the environmental chamber used for relative humidity studies: top panel-side view, and bottom panel-top view.

variation, and PTIR spectra are produced by plotting the resulting signal as a function of wavenumber. Under these typical conditions, acquiring a single PTIR spectrum over an individual particle takes approximately 10 minutes. For this study, to minimize damage to the particle, the OPO laser was operated at the lowest power that provided resolvable spectra, up to a maximum of 0.08 mW (0.9–3.0% power). Particle damage in a pure organic particle was not spectrally observable until the laser power reached 0.16 mW, as shown in Fig. S1 (see the ESI†).

AFM imaging of the laboratory generated aerosol particles were conducted at T = 298 K, and relative humidity (RH) of ~10–20% at ambient pressure. AFM images at a scan rate of 0.5 Hz using gold-coated silicon nitride probes (tip radius <30 nm) with 0.07–0.4 and 1–7 N m^{-1} spring constants, and 13 ± 4 and 75 ± 15 kHz resonant frequencies, in contact mode or tapping mode, respectively. Both probes have a lateral resolution of greater than 30 nm and allow for PTIR spectra acquisition, but vary in their imaging potential. In contact mode, the probe is left in contact with the sample and moved to a user-defined region, whereas in tapping mode, the probe

Published on 28 March 2018. Downloaded on 5/5/2026 1:00:26 AM.

is moved to a user defined location and then brought into contact with the sample. The probe is held in contact with the sample throughout the PTIR spectrum acquisition (loading force ~0.3–6.0 nN.) The contact mode probe allows for chemical and contact frequency mapping, whereas the tapping mode probe generates phase images. Photo-thermal IR spectra were collected with a spectral resolution of at least 8 cm^{-1}, averaging 128 laser pulses per wavenumber. All spectra shown were taken on a single point on the particle, without any averaging of spectra or smoothing filters applied. Unless denoted otherwise, spectra were collected at the highest point of the particle. Single wavenumber chemical maps are obtained by fixing the IR source to a single wavelength and irradiating the sample as the AFM raster scans. Chemical maps were collected at a scan rate of 0.05 Hz, averaging 16 times per pixel. For the water uptake measurements, the AFM head and the aerosol sample were contained within an environmental chamber system (Anasys Instruments, Santa Barbara, CA, USA) equipped with humidity and temperature sensor, a schematic of which is shown in Fig. 1b. The RH was adjusted by varying the ratio of wet and dry air controlled by a commercial dry air generator (Nano Purification Solutions, model NDC-600), across the range from 0 to 90% RH. RH sensor (Sensirion) inside the sample chamber was used to monitor the RH to within ±1%.

2.3. FTIR measurements: multi-analysis aerosol reactor

The FTIR extinction measurements of aerosol particles were performed on a Multi-Analysis Aerosol Reactor System (MAARS). Details of this apparatus have been described previously.[39,40] Briefly, the instrument is equipped with an aerosol generator, RH sensors, an IR extinction chamber with a path length of 78 cm which is positioned along the path of the IR beam (Thermo-Nicolet spectrometer, Nexus Model 670) equipped with a nitrogen liquid cooled MCT-A detector.

2.4. Volume equivalent diameters for substrate deposited particles and three-dimensional growth factors

To account for any particle deformation from impaction, aerosol particles sizes are reported as the diameter (D) of a sphere with equivalent volume (V).

$$D = \sqrt[3]{\frac{6V}{\pi}}$$

Following the method used by Morris *et al.*,[41] volume growth factors determined by AFM were quantified by taking the ratio of the volume equivalent diameters for the particle at a particular RH to that of the dry particle.[41]

$$\mathrm{GF_{vol}(RH)} = \frac{D_{\mathrm{vol}}(\mathrm{RH})}{D_{\mathrm{vol}}(\mathrm{Dry})}$$

3. Results and discussion

3.1. Single-component

3.1.1. Ammonium sulfate. Fig. 2a shows the 3D AFM height image of an ammonium sulfate particle (RH ~10%)

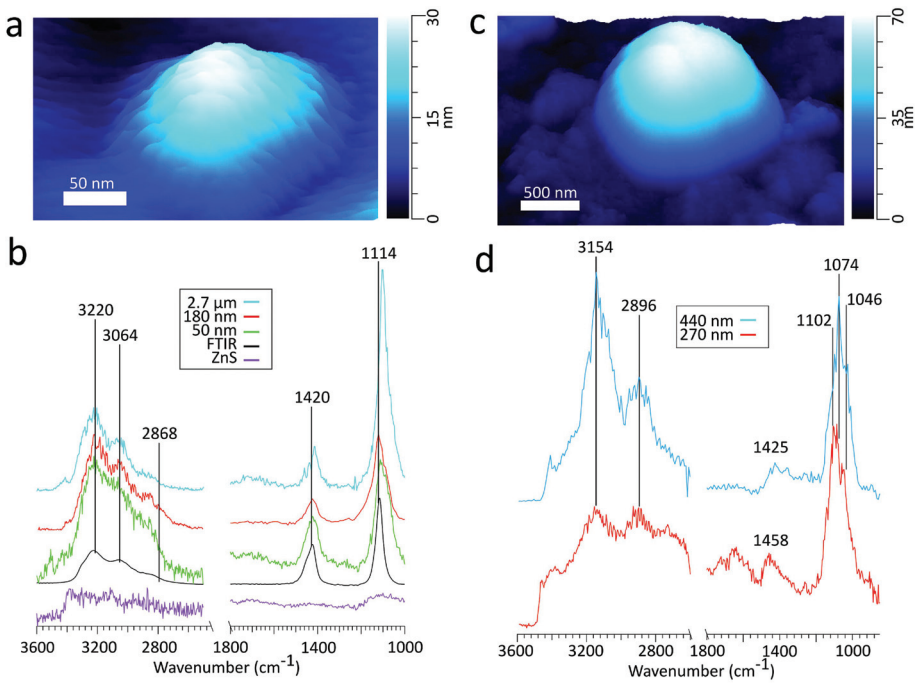

Fig. 2 (a) 3D height image of an ammonium sulfate particle on ZnS substrate with a volume equivalent diameter of 50 nm (b) comparison of the spectra obtained by FTIR (black) to PTIR for particles with volume equivalent diameters of varying sizes and the ZnS substrate. The peak frequencies in the figure correspond to the 180 nm sized particle. There is some variability in the peak frequencies, detailed in Table 2. (c) 3D height image of a glucose particle on ZnS substrate with a volume equivalent diameter of 270 nm. (d) PTIR spectra of glucose particles of varying sizes, denoted by the volume equivalent diameter.

 This journal is © The Royal Society of Chemistry 2018

Published on 28 March 2018. Downloaded on 5/5/2026 1:00:26 AM.

with a volume equivalent diameter of 50 nm on an IR inactive ZnS substrate. Fig. 2b shows the spectral region extending from 850 to 3600 cm^{-1}, the important spectral regions for ammonium sulfate infrared bands. The blue, red, and green spectra show the AFM-PTIR spectra obtained on single particles of 2.7 μm, 180 nm, and 50 nm in volume equivalent diameter, respectively. The black spectrum shows a comparison spectrum taken using FTIR extinction spectra of an ensemble of AS particles. A PTIR spectrum of the ZnS substrate is shown in purple. Both AFM-PTIR and FTIR spectra shows three of the four IR-active vibrational modes of the ammonium sulfate salt: $\nu_3(NH_4^+)$ (3230, 3064, 2868 cm^{-1}), $\nu_4(NH_4^+)$ (1424 cm^{-1}), and $\nu_3(SO_4^{2-})$ (1120 cm^{-1}), with peak comparisons summarized in Table 2.[42] The fourth vibrational mode of AS occurs at a frequency inaccessible by the tuning range of the OPO laser (below 850 cm^{-1}).

Table 2 compares peak intensity ratios between $\nu_4(NH_4^+)$ and $\nu_3(SO_4^{2-})$ vibrational modes across the various sized particles in PTIR and the FTIR spectra. The PTIR spectra for submicron particles yields $\nu_4(NH_4^+):\nu_3(SO_4^{2-})$ peak ratios of 1 : 3.1, 1 : 2.1, and 1 : 1.9 for the 180, 110, and 50 nm diameter particles, respectively. The ratios for the submicron particles (1 : 2.4 ± 0.9) are comparable to the peak ratio of 1 : 2.4 obtained for the FTIR spectra of an ensemble of particles. However, when examining the supermicron size regime, the 2.7 μm diameter particle gives a $\nu_4(NH_4^+):\nu_3(SO_4^{2-})$ peak ratio of 1 : 5.0, much larger than that of the submicron sized particles. Because PTIR signal depends on both the sample thickness and the absorbed energy per unit area (U_{abs}),[43] this deviation may be attributed to the nonlinearity of the PTIR technique beyond 1 μm in sample thickness and also differences in the power absorbed by the AS particle between the two wavelengths. Signal intensity at a given wavelength has been found to increase linearly with sample thickness up to ~1200 μm, and continues to increase nonlinearly with increasing thickness until reaching a wavelength dependent maximum.[44] The nonlinear behavior has been attributed to the exponentially decaying electric field in the sample at greater thicknesses. Additionally, in the supermicron particle, deviations in $\nu_4(NH_4^+):\nu_3(SO_4^{2-})$ peak ratios may arise from differences between the U_{abs} by the two vibrational modes, where U_{abs} is expected to be greater at $\nu_3(SO_4^{2-})$ mode due to a larger absorption coefficient and penetration depth relative to the $\nu_4(NH_4^+)$ mode.[45] Thus, even in the size regime where peak intensity growth is linear, the rate of growth may differ between the two vibrational modes. Comparing the relative intensities of these peaks with the $\nu_3(NH_4^+)$ mode is less straightforward due to the difference in the pulsed laser sources used in the two different regions.

Examining the PTIR spectrum for the 50 nm diameter AS particle, distinct peaks are present at $\nu_3(NH_4^+)$(3230, 3036, 2860 cm^{-1}), $\nu_4(NH_4^+)$ (1420 cm^{-1}), and $\nu_3(SO_4^{2-})$ (1112 cm^{-1}). The high signal from all vibrational modes suggests that chemical characterization can be conducted for particles on the sub-50 nm scale. AFM-PTIR spectroscopy is highly suitable for morphological and chemical characterization of particles around the size regimes necessary for both cloud condensation nuclei (CCN) and IN studies, where we demonstrate the capability to image and characterize particles across several magnitudes of atmospherically relevant size ranges.

3.1.2. Glucose. To demonstrate AFM-PTIR's ability to analyze organics, glucose particles deposited on a ZnS substrate were used. Fig. 2c shows the height image of a glucose particle with a 270 nm volume equivalent. Fig. 2d is the PTIR spectra taken on particles of various sizes, with the peak assignments described in Table 3.[46] The peak around 1640 cm^{-1} in the 270 nm sized particle can be attributed to residual water from the particle. In pure organics like glucose, the compounds are more viscous relative to inorganic salts,[26] making imaging in contact mode AFM more difficult as the sharp AFM tip will result in stronger particle tip–particle interactions that can lead to tip-induced particle movement or even tip-induced particle destruction. Some organic particles that have stronger intermolecular forces, or readily oligomerize, such as methylglyoxal can be imaged and studied using contact mode probes, shown in Fig. S2 (see the ESI†). For more fragile samples, operating AFM-PTIR in tapping mode is preferred to prevent damaging the sample. However, the spring constants differ by roughly one order of magnitude, with 0.07–0.4 and 1–7 N m^{-1} spring constants for contact and tapping mode probes, respectively. The larger spring constant in the tapping mode probe means that the cantilever deflection sensitivity to the photothermally induced particle expansions will be much lower than that for the more flexible contact mode tip.

Table 2 PTIR and FTIR of ammonium sulfate particles and peak intensity ratios between $\nu_4(NH_4^+)$ and $\nu_3(SO_4^{2-})$

	ν (cm^{-1})				
	PTIR				
Vibration	2.7 μm	180 nm	110 nm	50 nm	FTIR
$\nu_3(SO_4^{2-})$	1100	1120	1109	1112	1124
$\nu_4(NH_4^+)$	1412	1424	1426	1420	1420
$\nu_3(NH_4^+)$	2864	2868	2860	2860	2860
	3074	3064	3074	3064	3036
	3224	3220	3224	3216	3230
$\nu_4(NH_4^+):\nu_3(SO_4^{2-})$	1 : 5.0	1 : 3.1	1 : 2.1	1 : 1.9	1 : 2.4

Table 3 Peak assignments for glucose vibrational modes observed in AFM-PTIR spectroscopy

	ν (cm^{-1})	
Vibration	PTIR	Literature[46]
ν(CO) + ν (CC)	1046, 1074, 1102	1025, 1050, 1111
$\delta(CH_2)$ + δ(OCH) + δ(CCH)	1425, 1458	1382
ν_{as} (CH)	2896	2913
ν_s (CH)	2952	2944
ν(OH)	3144, 3408	3003, 3410

Published on 28 March 2018. Downloaded on 5/5/2026 1:00:26 AM.

3.2. Two-component mixed organic compounds and inorganic salts

3.2.1. Glucose mixed with sodium chloride. Shown in Fig. 3a and b is the height and phase image of a cluster of particles comprised of glucose and NaCl, wherein the particles exhibit a partially engulfed phase separated morphology at a 1 : 1 glucose : NaCl mass ratio.[26] Fig. 3c shows the PTIR spectra taken at two phase separated locations on the particle. The spectrum corresponding to the glucose-rich core corresponds well with the PTIR spectrum of the 270 nm glucose particle in Fig. 2d. Similar to the glucose particle, the broad peak at 1660 cm^{-1} is indicative of water content in the glucose-rich shell. The spectrum for the IR inactive NaCl-rich core shows significantly less intensity than that of the IR active glucose-rich shell. However, some signal from the core can be attributed to a thin layer of organic coating. Detection of thin organic coatings is possible, albeit less intense peaks are much less resolvable. While point spectra are useful for identifying species, it does not provide an explicit description of the spatial distribution of chemical species. AFM-PTIR provides single wavenumber chemical maps of materials with nanometer spatial resolution by irradiating the sample with the IR source tuned to a single wavelength throughout the AFM scan. Mapping wave numbers were selected by examining PTIR spectra for absorption frequencies exclusive or predominant for one region. A separate particle was imaged (Fig. 4a) and a chemical map was acquired at 1090 cm^{-1}, shown in Fig. 4b. In the chemical map, a majority of the signal at 1090 cm^{-1} arises from the ν(CO) + ν(CC) modes of the organic-rich glucose crown of the particle, while the IR inactive ZnS substrate and sodium chloride rich core remain relatively inactive. Compared to single-point spectra, chemical maps have far lower S/N, which is due to the significantly lower co-averaging used in chemical mapping, and thus was unable to detect any thin film organic coating on the NaCl-rich core. To obtain monolayer level sensitivity, more sophisticated methods such as resonance-enhanced AFM-PTIR are required.[47] AFM-PTIR chemical maps excel by providing nanoscale spatial distributions of chemical species. In previous studies, AFM analysis of organic volume fractions from AFM phase images operated under the assumption that the particle core is the inorganic component and the shell is the organic component.[26] With chemical maps, we explicitly demonstrate the organic and inorganic richness of the core and partially engulfing shell respectively.

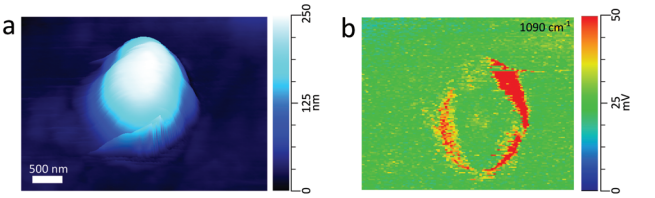

Fig. 4 (a) 3D height image of a glucose/NaCl (1 : 1 mass ratio) particle with a volume equivalent diameter of 510 nm (b) chemical map of the glucose rich regions of the particle taken at 1090 cm^{-1}.

3.2.2. Pimelic acid mixed with sodium chloride. Fig. 5 in panels a and b show the height and phase image, respectively, for a single 280 nm particle comprised of both PA and NaCl, with a partially engulfed phase separated morphology. Fig. 5c shows the IR spectra taken at the particle's different phase regions and on the ZnS substrate. The blue marker/spectrum is indicative of a region rich in pimelic acid, most identifiable by the distinct carbonyl stretch (1706 cm^{-1}). The red marker/spectrum corresponds to a region rich in sodium chloride, characterized by the lack of IR active bands. The small peak at around 1700 cm^{-1} likely due to a thin coating of pimelic acid. In the particle shown, no peaks corresponding to the sodium carboxylate salt were be observed. However, in a similar sized, homogeneous particle shown in Fig. S5 (see the ESI†), peaks corresponding to symmetric and asymmetric –COO stretches of the sodium-carboxylate salt[48] at 1410 and 1622 cm^{-1}

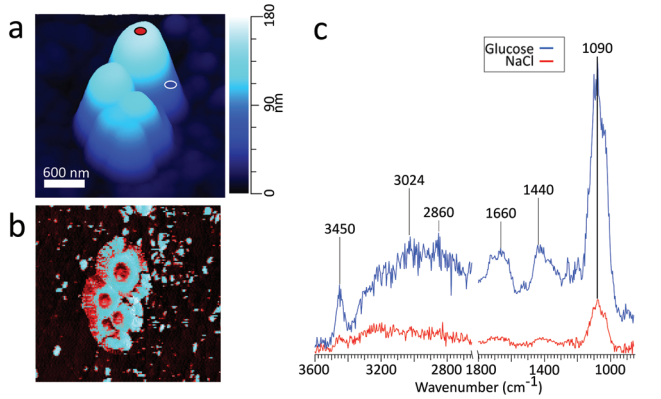

Fig. 3 (a) 3D height image of a cluster of glucose/NaCl (1 : 1 mass ratio) particles on ZnS substrate, with a volume equivalent diameter of 480 nm (b) phase image (c) PTIR spectra taken at NaCl-rich (red) and glucose-rich (blue) regions with the corresponding locations marked in panel (a).

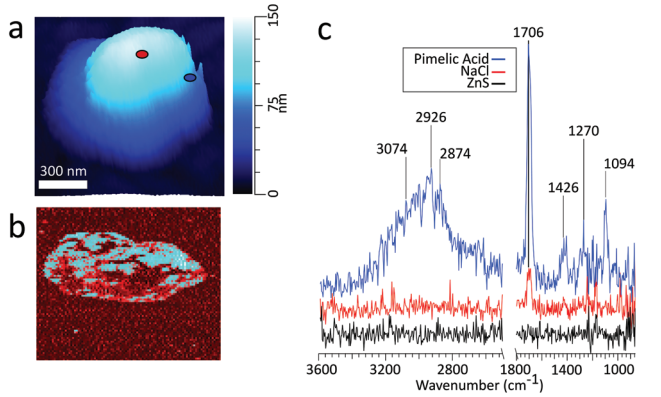

Fig. 5 (a) 3D height image of a PA/NaCl (1 : 1 mass ratio) particle with a volume equivalent diameter of 280 nm on ZnS substrate with markers identifying PTIR spectra locations (b) phase image (c) PTIR spectra obtained for PA rich (blue), NaCl rich (red) and ZnS (black) regions at the corresponding locations marked in panel (a).

This journal is © The Royal Society of Chemistry 2018

Published on 28 March 2018. Downloaded on 5/5/2026 1:00:26 AM.

respectively are observed. AFM and other microscopy techniques can probe the physical properties, morphology, and topography of aerosol particles, but AFM-PTIR adds the capability of correlating differences in physical properties or morphology with differences in chemical composition.

3.2.3. Pimelic acid mixed with ammonium sulfate. PA/AS particles were used to demonstrate AFM-PTIR's ability to study systems comprised of IR active inorganic salt and IR active organic compound, in contrast to the glucose/NaCl and PA/NaCl particles, which consisted of an IR inactive salt and IR active organic. Fig. 6a shows the AFM-PTIR spectra taken at different parts a particle comprised of pimelic acid and ammonium and on the ZnS substrate 280 nm away, with markers in Fig. 6d. The PA and AS particle shows two distinct IR signatures at different regions. The red marker/spectrum corresponds to ammonium sulfate-rich regions while the blue marker/spectrum is a region enriched with pimelic acid.

AFM-PTIR provides single wavenumber chemical maps of materials with nanometer spatial resolution by irradiating the sample with the IR source tuned to a single wavelength throughout the AFM scan. Mapping wavenumbers were selected by examining PTIR spectra for absorption frequencies exclusive or predominant for one region. The asymmetric sulfate stretch (1136 cm^{-1}) and carbonyl stretch (1698 cm^{-1}) were used to map for regions rich in pimelic acid and ammonium sulfate respectively, shown in Fig. 6b and c The most intensely absorbing regions arise from two distinct regions within the particle. This separation is more visible with an RGB overlay of the two maps in Fig. 6d which reveals a partially engulfed morphology. This chemical separation is consistent with cryo-TEM observations that observed phase separation between two species, but could not provide direct chemical distinction.[49] Chemical maps provide information on the distribution of chemical species and morphological assemblies, giving chemical context to the morphological and physical properties observed in other microscopy techniques.[32]

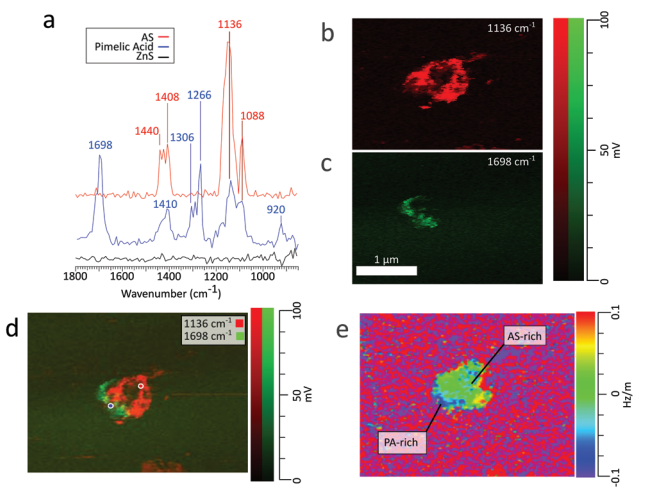

Fig. 6 (a) PTIR spectra obtained on a PA/AS particle for PA rich (blue) AS rich (red) and ZnS (black) regions at the corresponding locations marked in panel d. (b) Chemical image of the particle at 1136 cm^{-1} (c) chemical image of the particle at 1698 cm^{-1} (d) RGB overlay of chemical images in panels c and d. (e) Ratio image of the frequency map at 1136 cm^{-1} and height.

Frequency maps are simultaneously collected with chemical maps, which plot the contact resonant frequency of the cantilever as a function of spatial position, giving insight into differences in viscoelastic properties across a single particle. The contact resonance frequency for a given oscillation mode is dependent on the sample's mechanical properties, shifting to higher values as the stiffness or viscosity of the sample increases.[32] The dependency of these shifts on the sample's mechanical properties is similar to that of phase shifts in AFM tapping mode. Fig. 6e shows a ratio of the frequency to height images of the particle using the 1136 cm^{-1} frequency mapping. The ratio of the images was taken to show contrast the particle contact resonance frequency from the ZnS substrate. The ZnS substrate is IR transparent, so the substrate region shows no absorption features. Importantly, the collection of chemical and frequency maps is simultaneous and independent. Therefore, frequency maps can be compared directly with chemical maps to correlate chemical and mechanical properties. However, to obtain enough signal to extract physical properties from frequency mappings, the regions of interest must be IR active. Examining the frequency map acquired at 1698 cm^{-1}, shown in Fig. S6 (see the ESI†), reveals contact resonant frequencies for only the pimelic acid region of the particle. The region corresponding to ammonium sulfate has no IR active vibrational modes around 1696 cm^{-1} and gives no spectral features.

3.3. Hygroscopic studies: growth factors and spectroscopic signatures for water uptake

Extensive work has been done in measuring the water uptake of aerosol particles by using AFM to measure physical and morphological changes, such as surface tension, and growth factors. Currently, growth factors are the most straightforward metric for quantifying water uptake in AFM, where a single deposited particle is imaged at incrementally higher RH levels and the spherical diameter equivalent growth is calculated. NaCl is a well-studied system with a known deliquescence relative humidity (DRH) of 75.1 ± 1%.[50] For inorganic salts such as NaCl, prior to deliquescence there is no uptake of water vapor, and subsequently, there should be no change in particle size. Upon deliquescing, the phase changes from solid particle to aqueous droplet and should be accompanied by a significant increase in size and a corresponding decrease in viscosity.

Fig. 7a and b show a 1.3 µm dry volume equivalent diameter NaCl particle at 2% and 90% RH, respectively. Upon deliquescing, the particle grows in size and changes from a crystalline cubic solid to a droplet. Fig. 7c shows the growth factor and contact resonance frequency as a function of RH. Before the DRH, there is minimal change in growth factor and contact resonance frequency. However, above the DRH, a significant increase in the growth factor (1.0 to 2.2) and a concomitant decrease in the contact resonance frequency (260 to

Published on 28 March 2018. Downloaded on 5/5/2026 1:00:26 AM.

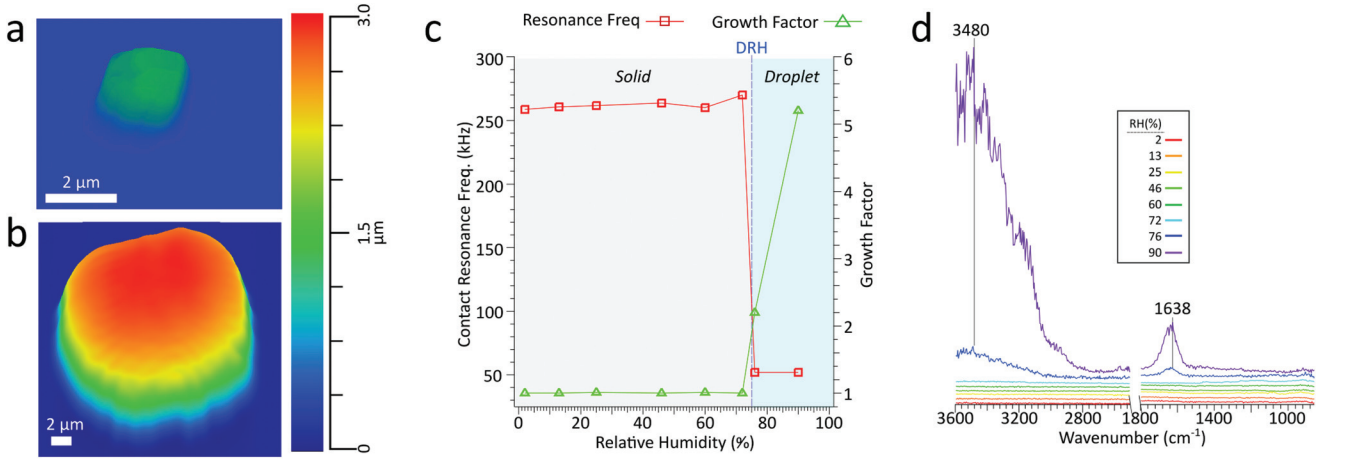

Fig. 7 (a) 3D height image of a NaCl particle with a volume equivalent diameter of 1.3 μm at 2% RH and (b) the same particle now with the diameter of 6.6 μm at 90% RH (c) contact resonance frequency (red) and growth factor (green) for the 1.3 μm NaCl particle as a function of increasing RH. Above the DRH (75%) there is a sharp increase in the growth factor and decrease in the contact resonance frequency. (d) PTIR spectra for the same particle as a function of increasing RH. Above the DRH, there is the growth in of two main peaks δ(OH) at 1638 cm^{-1} and ν(OH) at 3480 cm^{-1}, indicative of the absorbed water.

52 kHz), respectively, indicating that the particle has significantly increased in size and decreased in viscosity. Particle growth continues with increased water uptake at higher RH levels, the growth factor increases to 5.2. However, from 76% to 90% RH, there is no decrease in contact resonance frequency. Fig. 7d shows the PTIR spectra taken at increasing RH. Prior to the DRH of NaCl, at 75%, there is no absorbance from the IR inactive NaCl. Above the DRH, we observe the growth of two prominent absorbance bands at 1638 and 3480 cm^{-1}, the O–H bending and stretching modes, respectively, indicative of water absorption by the particle. In agreement with an increase in growth factor, the intensity of these two modes increases with increased water uptake at higher RH levels. Thus, we can conduct hygroscopic studies *via* single-particle measurements of particle size, stiffness, and chemical composition. While these results are for a supermicron sized NaCl particle, they lay the foundation for conducting similar studies in the submicron size regime, wherein, we can simultaneously observe changes in morphology, mechanical properties, and physical–chemical properties as a function of water vapor concentration.

To demonstrate PTIR spectra acquisition for deliquescence studies involving submicron sized particles, Fig. 8c shows PTIR spectra taken on a sodium chloride with a 135 nm dry volume equivalent diameter at 5% (red) and 85% RH (blue), with corresponding height images in Fig. 8a and b respectively. Beyond the DRH of NaCl, we still observe the stretching (3468 cm^{-1}) modes of the absorbed water. However, the lower intensity O–H bending mode was not discernible from noise. Similar to the supermicron-sized particle, at 85% RH we observe a 3D GF of 2.9, but no decrease in contact resonance frequency, which may occur due to the smaller particle size or contact with the substrate. The size dependence of this resonance frequency shift will be examined in more detail in future studies.

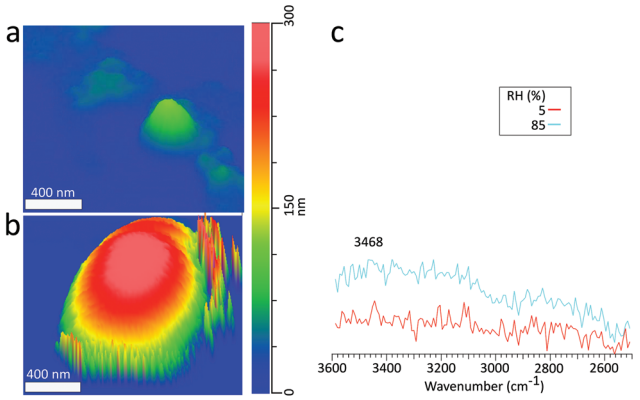

Fig. 8 (a) 3D height image a dry NaCl particle with a volume equivalent diameter of 140 nm on hydrophobic Si wafer substrate at 5%RH. (b) The deliquesced particle with diameter of 390 nm at 85% RH (c) PTIR spectra obtained on the particle marked in panel (a) and (b) at 5% RH (blue) and 85% RH (red).

3.4. Sample interactions with an IR active substrate

As infrared irradiation is not selective only to the aerosol particles, whenever the particle of interest is irradiated, the substrate also interacts with the incoming light. With an IR inactive substrate such as ZnS, there are no spectral deformations from the substrate absorbing IR light, but this differs when working with IR active substrates. Substrate thermal diffusivity, substrate–sample interactions, and substrate–IR radiation interactions are all potential issues that could result in particle deformations and spectral distortions. These concerns are especially important when working with an IR active substrate and increasingly smaller substrate deposited aerosol particles, which can be tens of nanometers in thickness. With smaller and subsequently thinner particles, potential interferences

 This journal is © The Royal Society of Chemistry 2018

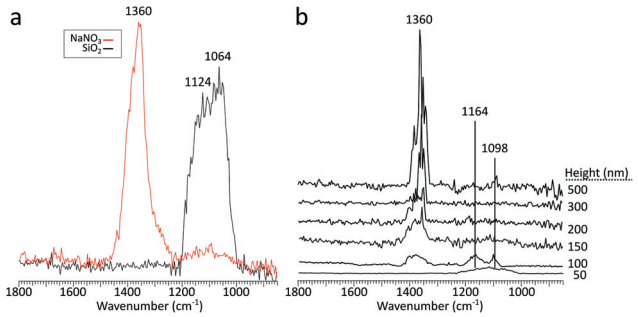

Fig. 9 (a) PTIR spectra obtained on a $NaNO_3$ particle (red) and silicon substrate (black), (b) PTIR spectra taken for particles of varying height.

Published on 28 March 2018. Downloaded on 5/5/2026 1:00:26 AM.

from the substrate absorbing IR light may arise. The thickness threshold for these interferences can be expected to vary between particles (and substrates) comprised of different chemical compositions and physical properties. As a preliminary assessment, sodium nitrate particles were deposited on a silicon wafer, SiO_2, which have a known absorbance around 1050 cm^{-1}.[51] Sodium nitrate has a known absorbance at roughly 1360 cm^{-1},[52] and was chosen due to the absence of any vibrational modes near 1100 cm^{-1}, making the presence of any substrate absorbances noticeably apparent.

For a reference, Fig. 9a shows the PTIR spectra of $NaNO_3$ in red and the substrate in black and Fig. 9b shows the PTIR spectra for particles of varying thickness. Below 200 nm thickness, there is a clear absorbance band from the substrate at 1100 cm^{-1}. While these impacts may be negligible for larger particles, when probing smaller particles, interference from an IR active substrate can produce noticeable spectral defects *via* substrate absorbance modes. In the 100 nm thick particle, the intensity of substrate and particle modes are comparable. Interestingly, in the 50 nm thick particle, no signatures from the particle were detectable. These defects were avoided in this study due to use of one (or a combination) of the following – an IR transparent substrate (ZnS), particle thickness much greater than 200 nm, or irradiating in spectral regions excluding the substrate absorption modes.

4. Conclusions

This study demonstrates AFM-PTIR spectroscopy to simultaneously measure the physicochemical and morphological properties of sub- and supermicron individual aerosol particles. The spectral information provided *via* single-particle AFM-PTIR spectroscopy is in a reasonably good agreement with traditional methods such as bulk FTIR. Moreover, we show that AFM-PTIR spectroscopy is a useful method to study multicomponent aerosol particles *via* chemical and frequency maps that provide high spatial resolution information on the spatial distribution of chemical species and their subsequent mechanical properties. We also show the chemical characterization of particles as small as 50 nm in diameter, as well as particles as large as 6.6 μm in diameter. The nanoscale resolution of AFM-PTIR allows us to study not only submicron sized particles interacting with water vapor but also interactions between water vapor and different regions within a single particle, which is vital for linking chemical composition to hygroscopic properties that describe the ability for an aerosol particle to act as effective CCN. Future hygroscopic studies with AFM-PTIR will focus on examining localized changes within a single multicomponent aerosol particle, wherein we can compare the behaviour of different components in response to reactive gas uptake and water vapor.

Conflicts of interest

There are no conflicts to declare.

Acknowledgements

The authors would like to thank Eoghan Dillon from Anasys Instruments and Professor Andrew Ault at the University of Michigan for helpful discussions. This work was supported by the National Science Foundation through the Centers for Chemical Innovation Program under Grant CHE1305427. The contents of this study do not necessarily reflect the official views of the National Science Foundation. NSF does not endorse the purchase of the commercial products used in this report.

References

1 U. Pöschl, *Angew. Chem., Int. Ed.*, 2005, **44**, 7520–7540.
2 V. F. McNeill, *Annu. Rev. Chem. Biomol. Eng.*, 2017, **8**, 427–444.
3 M. Hallquist, J. C. Wenger, U. Baltensperger, Y. Rudich, D. Simpson, M. Claeys, J. Dommen, N. M. Donahue, C. George, A. H. Goldstein, J. F. Hamilton, H. Herrmann, T. Hoffmann, Y. Iinuma, M. Jang, M. E. Jenkin, J. L. Jimenez, A. Kiendler-Scharr, W. Maenhaut, G. McFiggans, T. F. Mentel, A. Monod, A. S. H. Prévôt, J. H. Seinfeld, J. D. Surratt, R. Szmigielski and J. Wildt, *Atmos. Chem. Phys.*, 2009, **9**, 5155–5236.
4 N. Mahowald, D. S. Ward, S. Kloster, M. G. Flanner, C. L. Heald, N. G. Heavens, P. G. Hess, J.-F. Lamarque and P. Y. Chuang, *Annu. Rev. Environ. Resour.*, 2011, **36**, 45–74.
5 T. S. Bates, T. L. Anderson, T. Baynard, T. Bond, O. Boucher, G. Carmichael, A. Clarke, C. Erlick and H. Guo, *Atmos. Chem. Phys.*, 2006, **6**, 1657–1732.
6 N. Mahowald, D. S. Ward, S. Kloster, M. G. Flanner, C. L. Heald, N. G. Heavens, P. G. Hess, J.-F. Lamarque and P. Y. Chuang, *Annu. Rev. Environ. Resour.*, 2011, **36**, 45–74.
7 M. O. Andreae, *Nature*, 2001, **409**, 671–672.
8 A. Nel, *Science*, 2005, **308**, 804–806.
9 M. Subramanian, *Nature*, 2016, **534**, 166–169.
10 M. Shiraiwa, K. Ueda, A. Pozzer, G. Lammel, C. J. Kampf, A. Fushimi, S. Enami, A. M. Arangio, J. Fröhlich-Nowoisky, Y. Fujitani, A. Furuyama, P. S. J. Lakey, J. Lelieveld,

Published on 28 March 2018. Downloaded on 5/5/2026 1:00:26 AM.

K. Lucas, Y. Morino, U. Pöschl, S. Takahama, A. Takami, H. Tong, B. Weber, A. Yoshino and K. Sato, *Environ. Sci. Technol.*, 2017, **51**, 13545–13567.
11 K. Reinmuth-Selzle, C. J. Kampf, K. Lucas, N. Lang-Yona, J. Fröhlich-Nowoisky, M. Shiraiwa, P. S. Lakey, S. Lai, F. Liu, A. T. Kunert, K. Ziegler, F. Shen, R. Sgarbanti, B. Weber, I. Bellinghausen, J. Saloga, M. G. Weller, A. Duschl, D. Schuppan and U. Pöschl, *Environ. Sci. Technol.*, 2017, **51**, 4119–4141.
12 J. Schmale, D. Shindell, E. Von Schneidemesser, I. Chabay and M. Lawrence, *Nature*, 2014, **515**, 335–337.
13 S. China, C. Mazzoleni, K. Gorkowski, A. C. Aiken and M. K. Dubey, *Nat. Commun.*, 2013, **4**, ncomms3122.
14 R. E. Cochran, O. Laskina, J. V. Trueblood, A. D. Estillore, H. S. Morris, T. Jayarathne, C. M. Sultana, C. Lee, P. Lin, J. Laskin, A. Laskin, J. A. Dowling, Z. Qin, C. D. Cappa, T. H. Bertram, A. V. Tivanski, E. A. Stone, K. A. Prather and V. H. Grassian, *Chem*, 2017, **2**, 655–667.
15 K. A. Prather, T. H. Bertram, V. H. Grassian, G. B. Deane, M. D. Stokes, P. J. DeMott, L. I. Aluwihare, B. P. Palenik, F. Azam, J. H. Seinfeld, R. C. Moffet, M. J. Molina, C. D. Cappa, F. M. Geiger, G. C. Roberts, L. M. Russell, A. P. Ault, J. Baltrusaitis, D. B. Collins, C. E. Corrigan, L. A. Cuadra-Rodriguez, C. J. Ebben, S. D. Forestieri, T. L. Guasco, S. P. Hersey, M. J. Kim, W. F. Lambert, R. L. Modini, W. Mui, B. E. Pedler, M. J. Ruppel, O. S. Ryder, N. G. Schoepp, R. C. Sullivan and D. Zhao, *Proc. Natl. Acad. Sci. U. S. A.*, 2013, **110**, 7550–7555.
16 P. K. Quinn, D. B. Collins, V. H. Grassian, K. A. Prather and T. S. Bates, *Chem. Rev.*, 2015, **115**, 4383–4399.
17 L. M. Russell, R. Bahadur and P. J. Ziemann, *Proc. Natl. Acad. Sci. U. S. A.*, 2011, **108**, 3516–3521.
18 M. O. Andreae and A. Gelencsér, *Atmos. Chem. Phys.*, 2006, **6**, 3131–3148.
19 N. O. A. Kwamena, J. Buajarern and J. P. Reid, *J. Phys. Chem. A*, 2010, **114**, 5787–5795.
20 J. P. Darr, S. Q. Davis, Y. Kohno, K. McKenna and P. Morales, *J. Aerosol Sci.*, 2014, **77**, 158–167.
21 M. Song, C. Marcolli, U. K. Krieger, D. M. Lienhard and T. Peter, *Faraday Discuss.*, 2013, **165**, 289.
22 G. Binnig, C. F. Quate and C. Gerber, *Phys. Rev. Lett.*, 1986, **56**, 930–933.
23 V. H. Grassian, *J. Phys. Chem. Lett.*, 2015, **6**, 3880–3881.
24 X. Wang, C. M. Sultana, J. Trueblood, T. C. Hill, F. Malfatti, C. Lee, O. Laskina, K. A. Moore, C. M. Beall, C. S. McCluskey, G. C. Cornwell, Y. Zhou, J. L. Cox, M. A. Pendergraft, M. V. Santander, T. H. Bertram, C. D. Cappa, F. Azam, P. J. DeMott, V. H. Grassian and K. A. Prather, *ACS Cent. Sci.*, 2015, **1**, 124–131.
25 H. D. Lee, A. D. Estillore, H. S. Morris, K. K. Ray, A. Alejandro, V. H. Grassian and A. V. Tivanski, *J. Phys. Chem. A*, 2017, **121**, 8269–8305.
26 A. D. Estillore, H. S. Morris, V. W. Or, H. D. Lee, M. R. Alves, M. A. Marciano, O. Laskina, Z. Qin, A. V. Tivanski and V. H. Grassian, *Phys. Chem. Chem. Phys.*, 2017, **19**, 21101–21111.
27 H. D. Lee, K. K. Ray and A. V. Tivanski, *Anal. Chem.*, 2017, **89**, 12720–12726.
28 T. Hoffmann, R. J. Huang and M. Kalberer, *Anal. Chem.*, 2011, **83**, 4649–4664.
29 U. Dusek, G. P. Frank, L. Hildebrandt, J. Curtius, J. Schneider, S. Walter, D. Chand, F. Drewnick, S. Hings, D. Jung, S. Borrmann and M. O. Andreae, *Science*, 2006, **312**, 1375–1378.
30 I. Riipinen, T. Yli-Juuti, J. R. Pierce, T. Petäjä, D. R. Worsnop, M. Kulmala and N. M. Donahue, *Nat. Geosci.*, 2012, **5**, 453–458.
31 A. Dazzi, C. B. Prater, Q. Hu, D. B. Chase, J. F. Rabolt and C. Marcott, *Appl. Spectrosc.*, 2012, **66**, 1365–1384.
32 A. Dazzi and C. B. Prater, *Chem. Rev.*, 2017, **117**, 5146–5173.
33 A. Centrone, *Annu. Rev. Anal. Chem.*, 2015, **8**, 101–126.
34 A. L. Bondy, R. M. Kirpes, R. L. Merzel, K. A. Pratt, M. M. Banaszak Holl and A. P. Ault, *Anal. Chem.*, 2017, **89**, 8594–8598.
35 P. J. DeMott, A. J. Prenni, X. Liu, S. M. Kreidenweis, M. D. Petters, C. H. Twohy, M. S. Richardson, T. Eidhammer and D. C. Rogers, *Proc. Natl. Acad. Sci. U. S. A.*, 2010, **107**, 11217–11222.
36 G. C. Roberts, D. A. Day, L. M. Russell, E. J. Dunlea, J. L. Jimenez, J. M. Tomlinson, D. R. Collins, Y. Shinozuka and A. D. Clarke, *Atmos. Chem. Phys.*, 2010, **10**, 6627–6644.
37 K. J. Baustian, M. E. Wise and M. A. Tolbert, *Atmos. Chem. Phys.*, 2010, **10**, 2307–2317.
38 H. S. Morris, V. H. Grassian and A. V. Tivanski, *Chem. Sci.*, 2015, **6**, 3242–3247.
39 P. K. Hudson, E. R. Gibson, M. A. Young, P. D. Kleiber and V. H. Grassian, *Aerosol Sci. Technol.*, 2007, **41**, 701–710.
40 E. R. Gibson, P. K. Hudson and V. H. Grassian, *J. Phys. Chem. A*, 2006, **110**, 11785–11799.
41 H. S. Morris, A. D. Estillore, O. Laskina, V. H. Grassian and A. V. Tivanski, *Anal. Chem.*, 2016, **88**, 3647–3654.
42 D. D. Weis and G. E. Ewing, *J. Geophys. Res.*, 1996, **101**, 709–720.
43 A. Dazzi, F. Glotin and R. Carminati, *J. Appl. Phys.*, 2010, **107**, 124519.
44 B. Lahiri, G. Holland and A. Centrone, *Small*, 2013, **9**, 439–445.
45 M. E. Earle, R. G. Pancescu, B. Cosic, A. Y. Zasetsky and J. J. Sloan, *J. Phys. Chem. A*, 2006, **110**, 13022–13028.
46 M. Ibrahim, M. Alaam, H. El-Haes, A. F. Jalbout and A. De Leon, *Ecletica Quim.*, 2006, **31**, 15–21.
47 F. Lu, M. Jin and M. A. Belkin, *Nat. Photonics*, 2014, **8**, 307–312.
48 K. Ito and H. J. Bernstein, *Can. J. Chem.*, 1956, **34**, 170–178.
49 D. P. Veghte, D. R. Bittner and M. A. Freedman, *Anal. Chem.*, 2014, **86**, 2436–2442.
50 I. N. Tang and H. R. Munkelwitz, *Atmos. Environ., Part A*, 1993, **27**, 467–473.
51 I. W. Boyd and J. I. B. Wilson, *J. Appl. Phys.*, 1982, **53**, 4166–4172.
52 R. Newman, *J. Chem. Phys.*, 1952, **20**, 444–446.

 This journal is © The Royal Society of Chemistry 2018